J Eng Math (2014) 87:167–186
DOI 10.1007/s10665-013-9678-x

Detailed comparison of numerical methods for the perturbed sine-Gordon equation with impulsive forcing

Danhua Wang · Jae-Hun Jung · Gino Biondini

Received: 5 September 2012 / Accepted: 25 October 2013 / Published online: 20 March 2014

Abstract The properties of various numerical methods for the study of the perturbed sine-Gordon (sG) equation with impulsive forcing are investigated. In particular, finite difference and pseudo-spectral methods for discretizing the equation are considered. Different methods of discretizing the Dirac delta are discussed. Various combinations of these methods are then used to model the soliton–defect interaction. A comprehensive study of convergence of all these combinations is presented. Detailed explanations are provided of various numerical issues that should be carefully considered when the sG equation with impulsive forcing is solved numerically. The properties of each method depend heavily on the specific representation chosen for the Dirac delta—and vice versa. Useful comparisons are provided that can be used for the design of the numerical scheme to study the singularly perturbed sG equation. Some interesting results are found. For example, the Gaussian approximation yields the worst results, while the domain decomposition method yields the best results, for both finite difference and spectral methods. These findings are corroborated by extensive numerical simulations.

Keywords Finite difference methods · Impulsive forcing · Sine-Gordon equation · Spectral methods

1 Introduction

The sine-Gordon (sG) equation is a ubiquitous physical model that describes nonlinear oscillations in various settings such as Josephson junctions, self-induced transparency, crystal dislocations, Bloch wall motion of magnetic crystals, and beyond (see [1] for references). The sG equation is also an important theoretical model as it is a completely integrable system [2]. Many nonintegrable, nonlinear models also bear solitary wave solutions. In the specific case of the sG equation, these traveling wave solutions take the form of "kinks." Because various physical effects often result in the presence of localized defects or impurities, the interaction of such solutions with defects has been extensively studied in the literature [3–18]. In particular, the perturbed sG equation with the localized, nonlinear impulsive forcing, such as

$$u_{tt} - u_{xx} + \sin u = \epsilon\delta(x)\sin u, \quad u : \mathbb{R}^+ \times \mathbb{R} \to \mathbb{R}, \quad \epsilon \in \mathbb{R}^+, \tag{1}$$

also has been considered [3,7,9,10]. Henceforth, subscripts x and t denote partial differentiation with respect to space and time, respectively, $\delta(x)$ is the Dirac delta distribution [19], and ϵ is the forcing strength. Specifically, the

D. Wang · J.-H. Jung · G. Biondini (✉)
Department of Mathematics, State University of New York at Buffalo, Buffalo, NY 14260, USA
e-mail: biondini@buffalo.edu

Dirac delta forcing in (1) models the action of an attractive defect [5] for $\epsilon > 0$. To the best of our knowledge, the numerical treatment of (1) has not been adequately discussed in the literature. The issue is relevant because the Dirac delta is, of course, a distribution, and it is well known that the product of distributions is not, in general, a well-defined quantity. Even when one can show that the equation admits a unique (weak) solution, the presence of the impulsive forcing seriously affects the convergence of any numerical method used.

The purpose of this work is to address these issues by investigating and comparing the convergence properties of various numerical methods. Convergence is checked by determining the critical initial soliton velocity. Due to the singular property of the potential term of $\delta(x)$ and the critical solution behaviors of the sG equation, the convergence depends strongly on the representation of the Dirac delta. We provide in this paper a detailed explanation of various numerical issues that should be carefully considered when the sG equation with impulsive forcing is solved numerically.

In particular, we consider (1) finite-difference methods, both in time and space, and (2) spectral collocation methods (in space). In the nonlinear optics community, finite-difference methods have been most commonly used due to the simplicity and ease of handling the singular potential term. Spectral methods employ a global approximation, which may not be suitable for dealing with a singular term such as the Dirac delta. It is well known that, in the presence of such singularities, spectral methods yield oscillatory solutions. However, when appropriate regularization methods are adopted, spectral methods can be implemented efficiently and accurately, even for a singularly perturbed equation such as (1).

We have found that no single discretization method for the sG equation is the best in all cases. Instead, the properties of each method depend heavily on the specific representation chosen for the Dirac delta—and vice versa. For all cases, high resolution is required to capture the proper behavior of the critical soliton behaviors due to the singular potential. Spectral methods yield slightly better results than finite-difference methods when the domain decomposition method is used, but the overall convergence seems close to algebraic rather than exponential. The specific advantages and disadvantages of each method will be discussed.

Several different ways of representing the Dirac delta will be compared:

(a) Gaussian delta representation:

$$\delta_\sigma(x) = \frac{1}{\sigma\sqrt{2\pi}} \exp\left(-\frac{x^2}{2\sigma^2}\right), \tag{2}$$

which is the most commonly used regularization method in the existing literature to solve (1) and the nonlinear Schrödinger equation with a singular potential [9]. The idea is simply that if one chooses $\sigma \to 0$ and $N \to \infty$ (where $N + 1$ is the number of spatial grid points, as discussed in Sect. 3), $\delta_\sigma(x)$ converges to $\delta(x)$ in the distribution sense. This approach is popular because of its simplicity. However, due to the nonzero value of σ, the potential term always has a nonzero width, which affects the soliton dynamics. This results in a rather slow convergence for both the finite-difference and spectral methods, as discussed later.

(b) Point source:

$$\delta_{\text{ps}}(x) = \begin{cases} 0 & x \neq 0, \\ \delta_0 & x = 0, \end{cases} \tag{3}$$

with δ_0 chosen appropriately. The main advantage of this approach is that it is the simplest to implement, and such a definition yields a delta function of zero width on a discrete grid. By choosing the value of δ_0 for the given number of grid points properly, one can satisfy the normalization condition of the Dirac delta and mimic the local singularity on the grid. Due to these properties, our numerical results show that this crude regularization yields a good approximation, and even better results than the Gaussian regularization for both finite-difference and spectral methods. It is interesting to observe that spectral methods yield reasonable results with this point source approximation.

(c) Self-consistent delta representation. This approach is based on the fact that $\delta(x) = \mathrm{d}[H(x)]/\mathrm{d}x$ in the distribution sense, where $H(x)$ is the Heaviside step function [i.e., $H(x) = 0$ for all $x < 0$, $H(x) = 1/2$ for $x = 0$, and $H(x) = 1$ for all $x > 0$].

Numerically, this choice is realized by taking

$$\delta_\sigma(x) = \mathrm{D}\, H_\sigma(x),$$

where D is the numerical differentiation operator consistent with the spatial discretization of (1), and $H_\sigma(x)$ is a discrete representation of the step function. [For example, $H_\sigma(x) = 0$ for all $x \leq -\sigma$, $H_\sigma(x) = (1 + x/\sigma)/2$ for all $|x| < \sigma$, and $H_\sigma(x) = 1$ for all $x \geq \sigma$.] The discrete representation of $\delta_\sigma(x)$ based on this approach is oscillatory, but the resulting solution is without oscillations if the problem is linear. This approach is simple and consistent with the discretization method. Moreover, it is flexible enough that one can even choose a value of $\sigma = 0$. We will show that this approach yields better results than the Gaussian regularization.

(d) Domain decomposition. Using the continuity of $u(x, t)$ at $x = 0$ [namely, $u(0^+, t) = u(0^-, t), \forall t > 0$], (1) yields the following jump condition at $x = 0$:

$$u_x(0^+, t) - u_x(0^-, t) = -\epsilon \sin[u(0, t)]. \tag{4}$$

One then splits the domain $[-L, L]$ into two subdomains, $[-L, 0)$ and $(0, L]$, and solves numerically (1) with $\epsilon = 0$ in each subdomain, together with the jump condition (4). Thus, the domain decomposition approach does not involve a regularization of the Dirac delta, and the solutions in each subdomain are continuous in their derivatives. Thus one can expect that spectral methods will yield the most accurate result. However, compared to the previous discretization methods, this approach requires one to solve the additional Eq. (4). Moreover, when the kink is located near or at the interface, correctly reproducing the sharp transition in the kink profile may require a high resolution in order to avoid Gibbs oscillations. When the kink is trapped (i.e., localized near the defect), these spurious oscillations also affect the soliton behavior. As a result, even though this method has better accuracy, its overall convergence is not superior to that of other methods.

All of these representations are further discussed in Sect. 3. Note that (a) was used in [9] and (b) in [3], but neither discussed the numerical treatment of the partial differential equation (PDE). This paper will provide some useful guidelines on implementing numerically the singularly perturbed sG equation to study the critical behavior of its soliton solutions.

The outline of this paper is as follows. In Sects. 2 and 3 we discuss some mathematical and numerical preliminaries. In Sect. 4 we discuss finite-difference methods with the Gaussian delta, self-consistent delta, and point source methods. In Sect. 5 we do the same for the spectral collocation method. In Sect. 6 we discuss the domain decomposition method. Finally, in Sect. 7 we compare the results and offer some final remarks.

2 Mathematical preliminaries

2.1 Well-posedness

Equation (1) is posed with the boundary conditions (BCs) $u_x(\pm\infty, t) = 0$ for $t > 0$. Before attempting to solve it numerically, one must first address the issue of whether the problem is well-posed, namely, whether a unique solution exists that depends continuously on the initial condition (IC). A necessary requirement for well-posedness is to be able to assign an unambiguous meaning to the right-hand side of (1). This requires one to show that the product term of $\delta(x) \sin[u(x, t)]$ is well defined, at least in the distribution sense. In turn, this requires one to show that the preceding product, when multiplied by a test function and integrated over x from $-\infty$ to ∞, has a well-defined value. This last task is easily accomplished using any of the common representations of the Dirac delta, such as the box representation,

$$\delta_\sigma(x) = \begin{cases} 1/(2\sigma) & |x| < \sigma, \\ 0 & |x| \geq \sigma, \end{cases} \tag{5}$$

or the Gaussian delta representation (2). In both cases one has

$$\lim_{\sigma \to 0^+} \int_{-\infty}^{\infty} \delta_\sigma(x) f(x)\, \mathrm{d}x = \tfrac{1}{2} \left[f(0^+) + f(0^-) \right]$$

for all functions f in a suitable functional class [19], where $f(0^{\pm}) = \lim_{x\to 0^{\pm}} f(x)$. Also, for all $\sigma > 0$,

$$\int_{-\infty}^{\infty} \delta_\sigma(x)\,\mathrm{d}x = 1. \tag{6}$$

Replacing $\delta(x)$ with $\delta_\sigma(x)$ in (1), one obtains a forced nonlinear PDE that is easily shown to be well-posed. Denote its solution by $u_\sigma(x,t)$, and let $u(x,t) = \lim_{\sigma\to 0^+} u_\sigma(x,t)$. Next one shows that for $t > 0$

$$\lim_{\sigma\to 0^+} \int_{-\infty}^{\infty} \delta_\sigma(x) \sin[u_\sigma(x,t)] f(x)\,\mathrm{d}x = \tfrac{1}{2}\left\{\sin[u(0^+,t)] f(0^+) + \sin[u(0^-,t)] f(0^-)\right\},$$

in the same functional class, and that $u(x,t)$ solves the unperturbed sG equation

$$u_{tt} - u_{xx} + \sin u = 0 \tag{7}$$

for all $x \neq 0$, together with the continuity condition

$$u^+(0,t) = u^-(0,t) =: u(0,t) \tag{8}$$

and the jump condition (4). That is, $u(x,t)$ is continuous at $x = 0$, but $u_x(x,t)$ is discontinuous at $x = 0$, and (1) is well-posed in the sense that it admits a weak solution, albeit not a classical solution.

In this work we will represent the Dirac delta using the Gaussian delta representation, a point source, the self-consistent representation, or the domain decomposition method (see Sect. 3.3 for further details). One could use other representations, such as the "sinc" function: $\delta_\sigma(x) = \sin(x/\sigma)/(\pi x)$. This representation is not as convenient, however, because $\delta_\sigma(x)$ decays only weakly as $x \to \pm\infty$ [i.e., $\delta_\sigma(x) = O(1/x)$ as $x \to \pm\infty$], and $\lim_{\sigma\to 0^+} \delta_\sigma(x)$ does not exist for all finite $x \neq 0$. As a result, this representation applies in a much smaller functional class compared to the previous ones. For this reason we decided not to use it.

2.2 Behavior of perturbed solutions

The unperturbed sG equation [namely, (1) with $\epsilon = 0$] admits the well-known kink solution

$$u_o(x,t) = 4\arctan\{\exp[\nu m_o(x - X(t))]\}, \tag{9}$$

where $X(t) = V_o t + X_o$ is the kink position, V_o is its velocity, $\nu = \pm 1$ is the kink polarity, X_o is the initial position of the kink, and $m_o = 1/\sqrt{1 - V_o^2}$. Without loss of generality we take $\nu = 1$.

When $\epsilon \neq 0$, we take the IC to be the value of the kink solution (9) at $t = 0$, that is,

$$u(x,0) = u_o(x,0), \tag{10}$$

with $u_o(x,t)$ as previously. Since (1) is second-order in time, a second IC must be chosen. We then take

$$u_t(x,0) = u_1(x,0), \tag{11}$$

where

$$u_1(x,0) = \left.\frac{\partial u_o}{\partial t}\right|_{(x,0)} = -4 m_o V_o \arctan\{\exp[m_o(x - X_o)]\} \exp[-2 m_o(x - X_o)]. \tag{12}$$

There are then three possible outcomes: (a) particle pass, (b) particle reflection, and (c) particle capture [3], as illustrated schematically in Fig. 1a. That is, respectively: (a) the kink may either go through the impurity at $x = 0$ and continue to propagate, (b) it may bounce back – possibly after oscillating around the origin for a while – or (c) it may remain trapped forever in the region near the origin. Figure 2 shows the contour levels of the kink solution profiles as a function of time for a typical particle pass (a) and particle capture (b). The red region is the front of the kink solution [in which $u(x,t) \simeq 2\pi$], whereas the blue is the back of the kink solution [where $u(x,t) \simeq 0$].

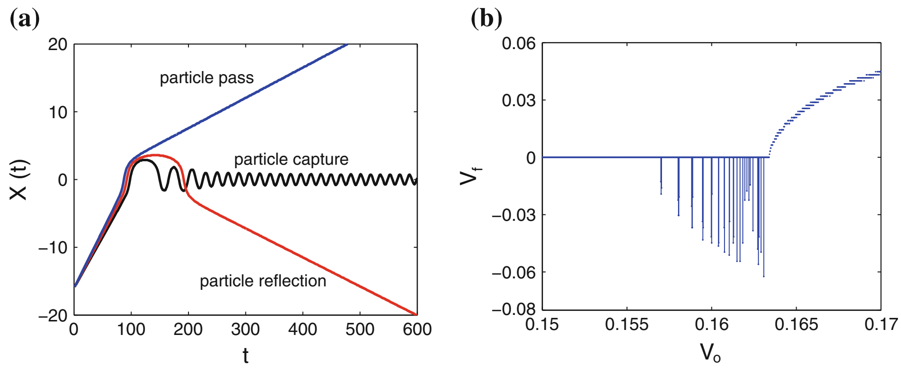

Fig. 1 **a** Particle coordinate $X(t)$ versus time for $\epsilon = 0.5$, showing the phenomena of particle pass, particle capture, and particle reflection. **b** Final kink velocity V_f as a function of the initial kink velocity V_o (the value $V_f = 0$ means that the kink is captured) as computed using the finite-difference method and a Gaussian delta representation, with discretization parameters $N = 2000$, $L = 80$, $\Delta t = 0.002$, and $\sigma = 0.1$

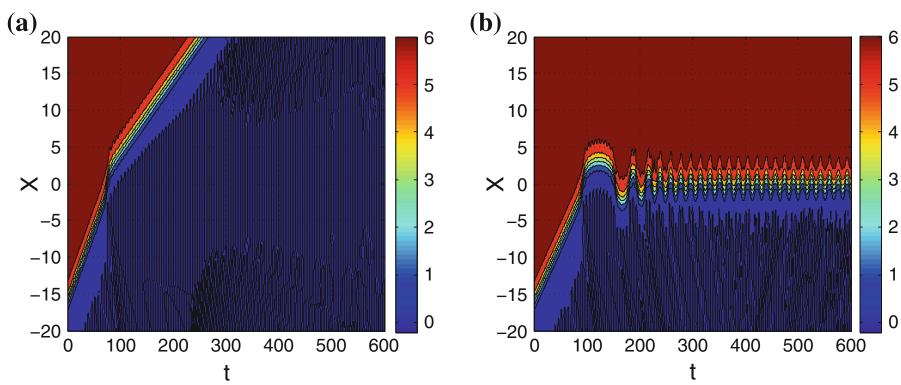

Fig. 2 Contour levels of solution as function of time, computed as Fig. 1 with $N = 1000$. (**a**): particle pass ($V_o = 0.2$). (**b**): particle capture ($V_o = 0.16$)

Denote by V_f the "final" velocity of the kink. In the case of particle pass or particle reflection, one may define the final velocity $V_f = \lim_{t\to\infty} V(t)$, where

$$V(t) = \frac{\mathrm{d}X}{\mathrm{d}t}, \qquad X(t) = \frac{1}{2\pi}\int_{-\infty}^{\infty} x\, u_x \,\mathrm{d}x \tag{13}$$

are the velocity of the kink and its mean position, respectively. The preceding definition, however, fails when the kink is trapped in a neighborhood of the origin, in which case there may be no limit value of $V(t)$. One can then give a more general definition of the final velocity as

$$V_f = \lim_{T\to\infty} \frac{1}{T}\int_0^T V(t)\,\mathrm{d}t = \lim_{T\to\infty} \frac{X(T) - X(0)}{T}. \tag{14}$$

This definition agrees with the previous one when the kink either passes through the impurity or is reflected by it. Note that the effect of the finite time interval in which the kink velocity is equal or approximately equal to V_o vanishes in the limit $T \to \infty$. Moreover, when the kink remains trapped, (14) yields $V_f = 0$.

The particular value of V_f obtained in each particular situation depends on the input velocity V_o, as shown in Fig. 1b, where the output velocity of the kink is plotted as a function of the input velocity. As is evident from Fig. 1b, the forced PDE (1) is characterized by a critical velocity $V_{cr} = V_{cr}(\epsilon)$, which is the smallest value such that each IC with $V_o > V_{cr}$ experiences particle pass.

3 Numerical preliminaries

3.1 Spatial and temporal discretizations

For all the numerical methods considered in this work, the solution of (1) will be computed by appropriately choosing $N + 1$ spatial grid points $x_0, \ldots, x_N$ in $[-L, L]$, with

$$-L = x_0 < x_1 < \cdots < x_{N-1} < x_N = L.$$

Letting Δt be the temporal step size and $t_k = k\Delta t$, with $K = T/\Delta t$ and $T = 600$, we take $u_n^k = u^{(\text{num})}(x_n, t_k)$ for $n = 0, \ldots, N$ and $k = 0, \ldots, K$. The superscript "(num)" denotes the numerical solution. Explicitly, for the finite-difference method, $x_n = -L + n\Delta x$, with $\Delta x = 2L/N$, while for the Chebyshev pseudo-spectral methods, x_n are the Chebyshev Gauss–Lobatto nodes, $x_n = -L\cos(n\pi/N)$ for $n = 0, \ldots, N$. Note that in all the simulations we will use *even* values of N, resulting in an odd number of spatial grid points, so that the point $x = 0$ is always part of the spatial grid: $x_{N/2} = 0$. As will be clear in Sect. 3.3, this is essential in ensuring a good numerical representation of the Dirac delta.

Since the goal is to compare the various methods with regard to the treatment of the space-dependent impulsive perturbation, the treatment of the spatial part is critically important [20]. Hence, for all the numerical methods we simply use finite differences to discretize the time derivative in (1). Specifically, we use the second-order centered difference stencil

$$\left.\frac{\partial^2 u_n}{\partial t^2}\right|_{t=t_k} = \frac{u_n^{k+1} - 2u_n^k + u_n^{k-1}}{\Delta t^2} + O(\Delta t^2). \tag{15}$$

The foregoing choice results in a leap-frog integration scheme, which is second-order with respect to time. After performing numerical tests, we verified that choosing $\Delta t \le 2 \times 10^{-4}$ produced an error of less than 10^{-4} on the critical velocity in all cases (see below for details), except when required by stability requirements resulting from the value of spatial step size Δx, in which case appropriately smaller values of Δt were chosen (see Sects. 4 and 5 for details).

3.2 Initial and boundary conditions

The aforementioned leap-frog method requires one to supply two starting values. Consistently with (10), for each numerical method we then impose

$$u_n^0 = u_o(x_n, 0), \qquad u_n^1 = u_o(x_n, 0) + \Delta t\, u_1(x_n, 0) \tag{16}$$

for all $n = 0, \ldots, N$. The value of X_o in (10) should be large enough to ensure that the results are not affected by the proximity of the kink to the origin at time $t = 0$. [Note that the value $X_o = -6$ used in [3] was not large enough to satisfy this criterion.] On the other hand, $X_o = -16$ (used in all the simulations presented in this work) was sufficiently large that the simulation results were unaffected by it. This was verified by checking that taking $X_o = -26$ did not change the results to a level of accuracy of 10^{-4}. Similarly, as we show later in more detail, the value $L = 80$ ensured that no boundary effects affected the solution at the specified level of accuracy, 10^{-4}, in any of the numerical methods used.

Recall that the PDE (1) is posed with the BCs $u_x(\pm\infty, t) = 0$. Numerically, at the left boundary of the computational domain (i.e., at $x = -L$) we impose the exact incoming BC

$$u(-L, t) = 4\arctan\{m_o \exp(-L - X_o - V_o t)\}, \quad 0 < t < T. \tag{17}$$

At the right boundary of the computational domain (i.e., at $x = L$) one has several choices. Here we impose the outflow BC

$$u_t(L, t) + u_x(L, t) = 0, \quad 0 < t < T, \tag{18}$$

so that if the kink propagates up to the edge of the computational domain, it continues to propagate, leaving the domain. Note that (18) is not a perfect outflow BC [21] because the final velocity of the kink (which is unknown a priori) is always different from 1 [which is the value that would result in a perfect transmission according to (18)]. As a result, if the kink reaches $x = L$, a small portion of it is reflected into the domain. This, however, does not affect the numerical results because in all the simulations described below, the output value of the kink is measured *before* the kink reaches the right edge of the computational domain.

3.3 Dirac delta discretization

As mentioned in Sect. 1, we consider several different ways to treat the Dirac delta numerically. We now provide further details for each method.

(a) *Gaussian representation* In this case, numerically one replaces $\delta(x)$ with representation (2), evaluated at the spatial grid points. It is useful to define two special subcases, which we denote as the three-point Gaussian and the five-point Gaussian. These are obtained by choosing σ such that the values obtained from (2) are nonnegligible at only three or five grid points, respectively. For finite differences, one can do this by taking $\sigma = \Delta x/2$ or $\sigma = \Delta x/\sqrt{2}$, respectively. In both cases, one has $\delta_\sigma(0) = 1/(\sqrt{2\pi}\,\sigma)$. In the first case, however, one has $\delta_\sigma(\pm\Delta x)/\delta_\sigma(0) = \mathrm{e}^{-2} \simeq 0.14$ and $\delta_\sigma(\pm 2\Delta x)/\delta_\sigma(0) = \mathrm{e}^{-8} \simeq 3.4\times 10^{-4}$. In the second case, instead, one has $\delta_\sigma(\pm\Delta x)/\delta_\sigma(0) = \mathrm{e}^{-1} \simeq 0.37$, $\delta_\sigma(\pm 2\Delta x)/\delta_\sigma(0) = \mathrm{e}^{-4} \simeq 0.018$ and $\delta_\sigma(\pm 2\Delta x)/\delta_\sigma(0) = \mathrm{e}^{-9} \simeq 1.2\times 10^{-4}$. The choice of σ for pseudo-spectral methods follows similar considerations, except that one needs to take into account that in that case the grid spacing is nonuniform and is largest at the origin. Specifically, $\Delta x_{N/2} = x_{N/2+1} - x_{N/2} = x_{N/2} - x_{N/2-1} = L\sin(\pi/N) \simeq L\pi/N$ is the grid spacing on either side of the origin. Therefore, in this case we define the three- and five-point Gaussians as those obtained respectively with $\sigma = \pi L/(2N)$ and $\sigma = \pi L/(\sqrt{2}\,N)$.

(b) *Point source* This is a special limit of the box representation (5) in which $\delta_\sigma(x_n) \neq 0$ only at the central grid point, $x_{N/2} = 0$. Specifically, one uses (5), with $\sigma = \Delta x_{N/2}/2$, where again $\Delta x_{N/2}$ is the grid spacing to the left and the right of the origin. All the spatial discretizations used in this work result in spatial grids that are symmetric around the origin. In this way one has $\delta_\sigma(x_n) = 0$ for all $n \neq N/2$ and $\delta_\sigma(x_n) = \delta_0$ for $n = N/2$. The value of δ_0 is then chosen so that the perturbation is properly normalized, $\delta_0 = 1/\Delta x_{N/2}$, which ensures that (6) is satisfied.

(c) *Self-consistent representation* Mathematically one writes $\delta_\sigma(x) = \mathrm{d}[H_\sigma(x)]/\mathrm{d}x$, where $H_\sigma(x)$ is a representation of the Heaviside step function: $H(x) = 0$ for all $x > 0$, $H(x) = 1/2$ for $x = 0$, and $H(x) = 1$ for all $x > 0$. Numerically, this choice is realized by taking $\delta_\sigma(x) = \mathrm{D}\,H_\sigma(x)$, where D is the numerical differentiation operator consistent with the spatial discretization and $H_\sigma(x)$ is a discrete representation of the step function. Explicitly,

$$\delta_\sigma(x_n) = \sum_{m=0}^{N} \mathrm{D}_{n,m} H_m, \tag{19}$$

where $H_n = H_\sigma(x_n)$ for $n = 0, 1, \ldots, N$. We use the "tanh" representation for H_σ

$$H_\sigma(x) = \tfrac{1}{2}\big(1 + \tanh(x/\sigma)\big). \tag{20}$$

As $\sigma \to 0$, it is obvious that $H_\sigma(x) \to H(x)$.

(d) *Domain decomposition* As explained earlier, (1) is equivalent to (7) for all $x \neq 0$, together with the jump condition (4). Numerically, one solves (7) on the two spatial domains $[-L, 0)$ and $(0, L]$, and the jump condition (4) becomes a BC for each domain. The jump condition has two effects: (1) it couples the solutions in the two domains; (2) it provides an implicit equation for $u(0, t)$, which allows one to update the value of the solution at the origin, $u^k_{N/2} = u(0, t_k)$. The precise way in which this second step is realized will be discussed in Sect. 6.

Note that the Gaussian delta representation and the self-consistent delta introduce the additional discretization parameter σ, while the point source model and the domain decomposition have no such free parameter.

3.4 Critical velocity and validation

Each numerical method will produce an estimate of the critical velocity that in general depends on the values of the discretization parameters. For example, if the finite difference method is used in conjunction with the Gaussian representation, one has $V_{\rm cr}^{(\rm num)} = V_{\rm cr}(\epsilon; L, N, \Delta t, \sigma)$. A similar situation arises for all other numerical methods. An obvious and important question is then whether, for each method, $V_{\rm cr}^{(\rm num)}$ converges to $V_{\rm cr}$ as the discretization parameters $1/N$, Δt, σ tend to 0, and, if so, how quickly. In this work we compare the various numerical methods with respect to this criterion.

Let us discuss the algorithm used to numerically reconstruct the kink position $X(t)$ as a function of time. Numerically, we define $X(t)$ as the position of the half-value of the kink. In order to determine $X(t)$ at time t, we consider the maximum value $u_{\max}(t) = \max_{x\in[-L,L]} u(x,t)$ and the minimum value $u_{\min}(t) = \min_{x\in[-L,L]} u(x,t)$ of the solution. We calculate the average of these values, $u_{\rm avg} = (u_{\min} + u_{\max})/2$. We then find the numerical solution value closest to the average value, and we take the corresponding x-coordinate of this closest value to be the kink position $X(t)$. While one could obviously use much more sophisticated procedures, the above-described algorithm is very fast, and, in most cases, it captures the kink position quite well. The algorithm fails occasionally when large amounts of dispersive radiation are generated. However, this only happens when the kink is reflected, and therefore the failure of the algorithm does not affect the results about the value of the critical velocity. Other options were also tried, such as the numerical evaluation of (13), but the corresponding results had a comparable level of accuracy to those with the above method.

Finally, from the kink position $X(t)$ we obtain the output velocity $V_{\rm f}$. Specifically, we define $V_{\rm f}$ as the average velocity for the last 50 measured values of $X(t)$. We then repeat the simulations for many, finely spaced values of $V_{\rm o}$, and we take the numerically determined $V_{\rm cr}$ to be the greatest lower bound of the set of the initial velocities such that $X(T) = 6$. We use the value of $V_{\rm cr}^{(\rm num)}$ obtained from the most accurate simulations—namely, those with the largest number of grid points—to be our estimate for $V_{\rm cr}$. This results in the previously quoted value $V_{\rm cr} = 0.1657$.

The last issue that must be discussed is the uncertainty in the preceding value of $V_{\rm cr}$. We should emphasize that the accuracy of $V_{\rm cr}$ is *not* affected by the uncertainty in the measurement of $V_{\rm f}$ because the critical velocity is an *input* velocity, not an output one. Here *input velocity* means the input velocity of the kink before the kink reaches the impurity, whereas *output velocity* means the velocity of the kink after the kink has interacted with the impurity. In other words, note from Fig. 1b that $\mathrm{d}V_{\rm f}/\mathrm{d}V_{\rm o} \to \infty$ as $V_{\rm o} \to V_{\rm cr}$ from the right. Thus, the uncertainty in the value of $V_{\rm cr}$ is simply determined by how accurately one can measure input velocities. Accordingly, the uncertainty in the estimate of $V_{\rm cr}$ was taken to be the upper limit of the difference between the input velocity of a kink and its measured velocity when $\epsilon = 0$. As discussed in more detail in the following sections, for each numerical method the parameters L, N, Δt, and $X_{\rm o}$ were chosen such that this uncertainty was always less than 10^{-4}, implying that the simulations allow one to estimate the critical velocity with four significant digits after the decimal point. Correspondingly, the input velocities used in the simulations were chosen such that the difference between consecutive values of $V_{\rm o}$ was $\Delta V_{\rm o} \simeq 10^{-4}$.

4 Finite-difference methods

4.1 Implementation

As mentioned earlier, we use a spatial grid size $\Delta x = 2L/N$, and we take the grid points to be $x_n = -L + n\Delta x$ for $n = 0, 1, \ldots, N$. Taking $u_n^k = u^{(\rm num)}(x_n, t_k)$, discretizing (1), and utilizing the three-point, second-order centered stencil for the second spatial derivative, we obtain, for all $k \geq 1$ and $n = 1, 2, \ldots, N-1$,

$$\frac{u_n^{k+1} - 2u_n^k + u_n^{k-1}}{\Delta t^2} - \frac{u_{n+1}^k - 2u_n^k + u_{n-1}^k}{\Delta x^2} + [1 - \epsilon\delta_\sigma(x_n)] \sin u_n^k = 0. \tag{21}$$

The IC and the left BC are specified by simply imposing (16) and (17), as discussed in Sect. 3. At the right boundary, we discretize (18) with the explicit scheme

$$\frac{u_N^{k+1} - u_N^k}{\Delta t} + \frac{u_N^k - u_{N-1}^k}{\Delta x} = 0. \tag{22}$$

The Courant-Friedrichs-Lewy stability criterion for the foregoing scheme is $\Delta t < \Delta x = 2L/N$. A more stringent requirement on the temporal step size, however, is provided by the need to preserve accuracy, as we discuss in the following sections. As mentioned earlier, one can obtain an upper bound for the error in the determination of the critical velocity by simply taking the difference between the numerically determined velocity of a kink in the case $\epsilon = 0$ and that of the exact analytical solution. When applying the foregoing finite-difference scheme to the unperturbed sG equation, we find that the error in the numerically determined kink velocity is 10^{-4} or less when $L = 80$, $\Delta t = 2 \times 10^{-4}$, and $N \geq 4{,}000$. With these constraints, we then proceed to test the various representations of the Dirac delta.

4.2 Perturbed kink behavior with finite differences

We first test the finite-difference method with the Gaussian delta. As explained in Sect. 3.3, when using the Gaussian representation of the Dirac delta one simply replaces $\delta(x)$ with $\delta_\sigma(x_n)$, as given by (2). Figure 4a shows the numerically determined critical velocity as a function of N and σ when all other discretization parameters are sufficiently small that the corresponding numerical errors are smaller than 10^{-4}, which can therefore be neglected. Figure 4b shows the dependence of the absolute error $E = |V_{\text{cr}}^{(\text{num})} - V_{\text{cr}}|$ on N and σ. The continuum limit corresponds to the limit $(1/N, \sigma) \to 0$, which is the point at infinity in the direction of the lower left corner of either plot. The error should therefore vanish in this limit. Indeed, Fig. 4b shows that, if one takes the limit $N \to \infty$ while σ is fixed, then $V_{\text{cr}}^{(\text{num})}$ converges to a finite value, which in turn converges to V_{cr} as $\sigma \to 0$. On the other hand, if one decreases σ while N is fixed, then $V_{\text{cr}}^{(\text{num})}$ increases, and no finite critical velocity emerges, in the sense that eventually $V_{\text{cr}}^{(\text{num})} \to 1$, and the system ceases to display any particle passes. This behavior can be easily explained by recalling that $\Delta x = 2L/N$. Thus, when $\sigma \ll L/N$, the perturbing term in the numerical method becomes effectively a point source because the Gaussian has nonnegligible values only at the central grid point. In that case, however, the source term is not normalized correctly because when $\sigma \ll \Delta x$, it is

$$\int_{-\infty}^{\infty} \delta_\sigma(x)\,\mathrm{d}x \simeq \sum_{n=0}^{N-1} \delta_\sigma(x_n)\Delta x \simeq \frac{\Delta x}{\sigma\sqrt{2\pi}} \neq 1.$$

In fact, the right-hand side of the preceding equation tends to infinity as $\sigma \to 0$, with Δx fixed, meaning that in this limit the perturbation to the sG equation grows to an infinite strength.

The foregoing discussion demonstrates that, as with the limit $(\Delta x, \Delta t) \to 0$, one must be careful when taking the limit $(1/N, \sigma) \to 0$ to recover the correct PDE behavior. In particular, when using the Gaussian delta representation, we see that the three-point Gaussian is not convergent, and one needs to take at least the five-point Gaussian to recover the correct behavior in the limit $N \to \infty$.

Next we test the finite-difference method with the self-consistent delta. As discussed earlier, this choice is realized by replacing $\delta(x)$ in (21) with (19). In particular, the differentiation matrix obtained from the second-order centered difference stencil yields

$$\delta_\sigma(x_n) = \begin{cases} (H_\sigma(x_1) - H_\sigma(x_0))/\Delta x & n = 0, \\ (H_\sigma(x_{n+1}) - H_\sigma(x_{n-1}))/2\Delta x & n = 1, \ldots, N-1, \\ (H_\sigma(x_N) - H_\sigma(x_{N-1}))/\Delta x & n = N. \end{cases}$$

Note that, even though the first and last values in the preceding equation are obtained from a one-sided stencil, these values are not used in (21) since the solution at the first and last grid points are updated using the BCs.

As before, Fig. 5 shows the dependence on N and σ of the numerical critical velocity and the absolute error. Again, if σ is fixed while N is increased, $V_{\rm cr}^{\rm (num)}$ converges to a finite value, which in turn converges to $V_{\rm cr}$ as $\sigma \to 0$. Contrary to the case of the Gaussian delta, however, if σ is decreased while N is fixed, $V_{\rm cr}^{\rm (num)}$ still converges to a finite value. This is related to the fact that, unlike the Gaussian delta, even when $\sigma = 0$, the perturbation is not a point source, as can be seen in Fig. 3, and it is still normalized correctly. The error floor at the bottom left corner of Fig. 5b is due to the fact that we only keep four significant digits for the value of critical velocity.

Finally, we use the point source representation of the Dirac delta, taking $\sigma = \Delta x/2$ in (5). Recall from Sect. 3.3 that in this case there is no extra Dirac delta discretization parameter. Hence, in this case Fig. 6 simply shows the dependence on N of the numerical critical velocity $V_{\rm cr}^{\rm (num)}$ and the absolute error $E = |V_{\rm cr}^{\rm (num)} - V_{\rm cr}|$. In this case we find that $V_{\rm cr}^{\rm (num)}$ already converges to the correct value when $N = 4{,}000$. As in the case of the self-consistent delta, the error floor at 10^{-4} is a consequence of the fact that we only have four significant digits.

As shown in Figs. 4–6, the point source and self-consistent approximation approaches yield better performance than the Gaussian approach. In particular, it is interesting that the point source works well. The overall order of convergence from Fig. 6 is approximately 2.3.

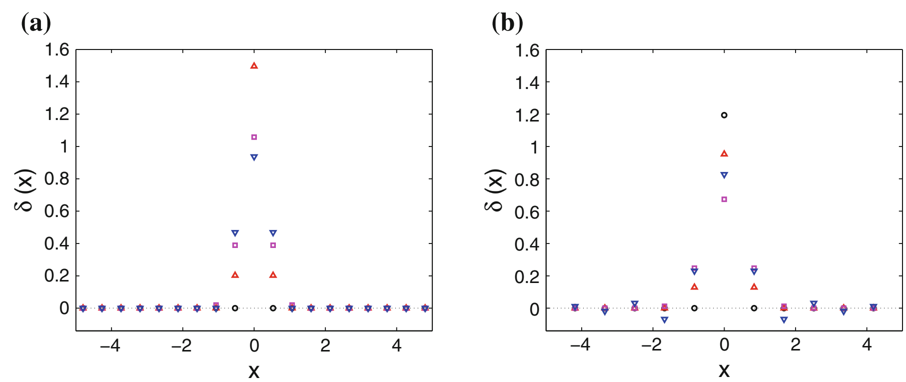

Fig. 3 Numerical representations of Dirac delta on finite interval $[-L, L]$ with $L = 80$ and $N = 300$ with an equally spaced grid (**a**) and on a grid of Gauss–Lobatto nodes $x_n = -L\cos(n\pi/N)$ (**b**): five-point Gaussian (*magenta*), three-point Gaussian (*red*), point source (*black*), self-consistent with $\sigma = 0$ (*blue*) with second-order centered differences (**a**) or Chebyshev differentiation matrix (**b**). (Color figure online)

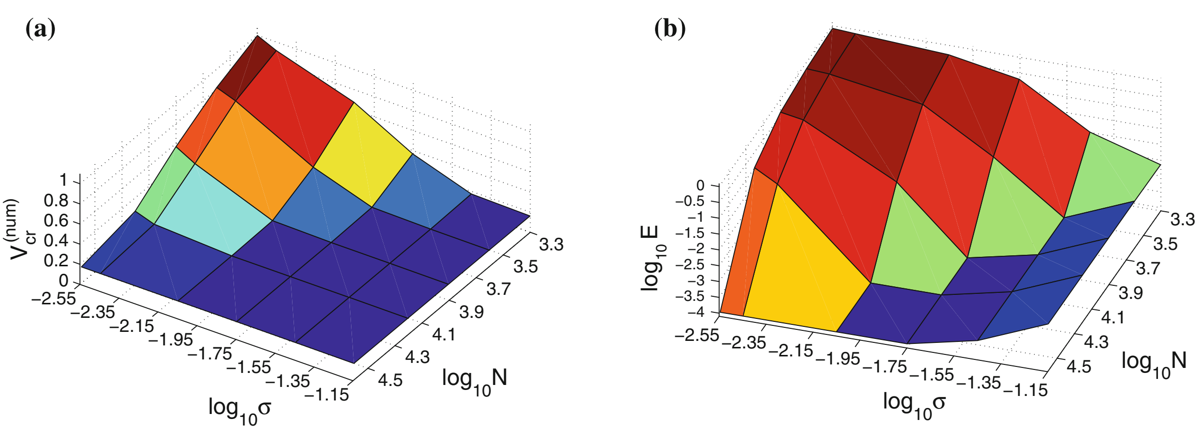

Fig. 4 Numerical critical velocity $V_{\rm cr}^{\rm (num)}$ (**a**) and absolute error $E = |V_{\rm cr}^{\rm (num)} - V_{\rm cr}|$ (**b**) for finite-difference method with Gaussian delta as a function of N and σ

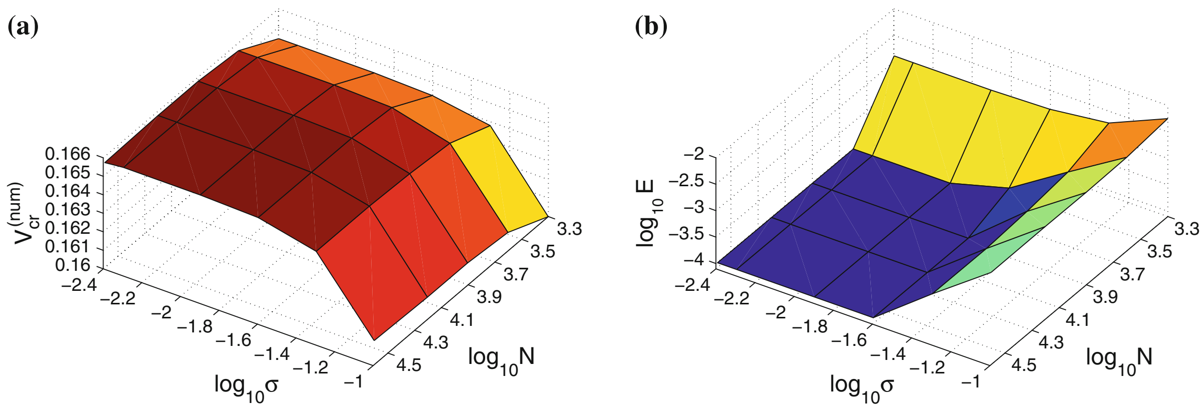

Fig. 5 Same as Fig. 4, but for the finite-difference method with self-consistent delta

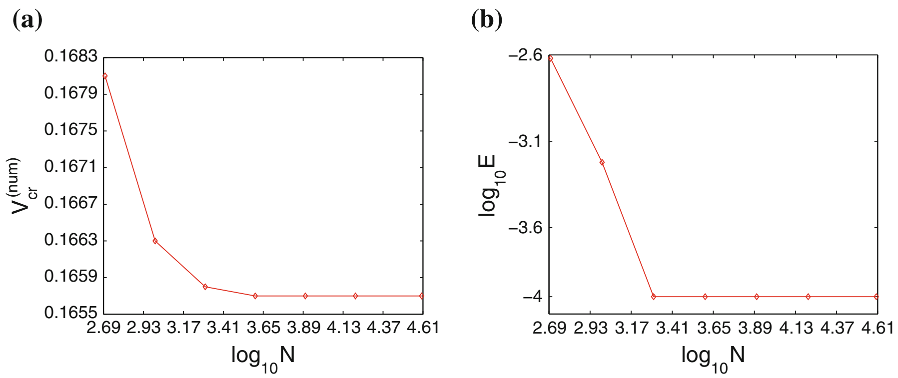

Fig. 6 Numerical critical velocity $V_{\text{cr}}^{(\text{num})}$ (**a**) and absolute error $E = |V_{\text{cr}}^{(\text{num})} - V_{\text{cr}}|$ (**b**) for finite-difference method with point source as a function of N

5 Pseudo-spectral method

5.1 Implementation

We use the Chebyshev spectral collocation method, taking the x_n to be the Gauss–Lobatto quadrature points and using the Lagrange interpolation polynomial to approximate the solution of the perturbed sG equation (1):

$$u^{(\text{num})}(x, t) = \sum_{n=0}^{N} \hat{u}_n(t)\phi_n(x), \tag{23}$$

where $\phi_0(x), \ldots, \phi_N(x)$ are the Chebyshev polynomials [22–26]:

$$\phi_n(x) = T_n(\xi(x)), \qquad n = 0, \ldots, N,$$

where $\xi(x) = x/L$ maps the interval $[-L, L]$ to $[-1, 1]$, and

$$T_{n+1}(\xi) = 2\xi T_n(\xi) - T_{n-1}(\xi) \qquad \forall n \in \mathbb{N},$$

with $T_0(\xi) = 1$ and $T_1(\xi) = \xi$. The value of the solution at all spatial grid points at the kth time step forms the column vector

$$\mathbf{u}^k = (u_0^k, \dots, u_N^k)^{\mathrm{T}}, \tag{24}$$

with $u_n^k = u^{(\mathrm{num})}(x_n, t_k)$.

We then discretize (1) in both time and space using the Chebyshev differentiation matrix for the spatial derivative and central differences for the time discretization,

$$\frac{\mathbf{u}^{k+1} - 2\mathbf{u}^k + \mathbf{u}^{k-1}}{\Delta t^2} - \mathrm{D}_N^2 \mathbf{u}^k + \left(I_N - \epsilon\, \delta_N\right) \sin \mathbf{u}^k = 0. \tag{25}$$

Here I_N is the $(N+1) \times (N+1)$ identity matrix, $\delta_N = \mathrm{diag}(\delta_\sigma(x_0), \dots, \delta_\sigma(x_N))$, and D_N^2 is the $(N+1) \times (N+1)$ second-order Chebyshev differentiation matrix, which allows one to express the values of $u_{xx}(x,t)$ at the spectral collocation points as a function of $u_0^k, \dots, u_N^k$ [22–26].

As with the finite-difference method, the IC is specified by assigning u_n^0 and u_n^1 according to (10), and the left BC is specified by assigning u_0^k according to (17). Finally, for the right boundary, similarly to (22), we discretize (18) with the explicit scheme

$$\frac{u_N^{k+1} - u_N^k}{\Delta t} + \frac{u_N^k - u_{N-1}^k}{x_N - x_{N-1}} = 0.$$

To avoid blow-up, one needs $\Delta t < \Delta x$. The grid spacing is nonuniform, and one should take

$$\Delta x = \min_{n=1,\dots,N} \{x_n - x_{n-1}\} = x_N - x_{N-1} = x_1 - x_0 = L\,(1 - \cos(\pi/N)) \simeq \frac{L\pi^2}{2N^2}. \tag{26}$$

Hence, in this case $\Delta t = O(1/N^2)$. Note that the coefficients $\hat{u}_0(t), \dots, \hat{u}_N(t)$ of the Chebyshev polynomials in (23) are never used in practice in the numerical solution of the PDE.

As before, we test the Chebyshev spectral collocation method on the unperturbed sG equation (7) to quantify the numerical error of the numerically measured velocity of the kink solution. We find that the error is less than 10^{-4} when $L = 80$ and $N = 500$. As before, with these constraints we then proceed to test the various discretizations of the Dirac delta.

Recall that the Chebyshev polynomials on the Gauss–Lobatto points, $x_j = -\cos(j\pi/N)$ for $j = 0, \dots, N$, are basically cosine functions. That is,

$$T_l(x_j) = \cos(l \cos^{-1}(x)) = \cos(l \cos^{-1}(\cos(j\pi/N))) = \cos(lj\pi/N).$$

Thus the derivative of $u(x,t)$ for any derivative order based on the matrix vector multiplication can be efficiently implemented via the fast Fourier transformation (FFT).

Equivalently, one can also implement a spectral Galerkin method using a Galerkin projection. The difference is that the Galerkin projection can directly project the Dirac delta, which is computed easily using the definition of the δ-function for the one-domain approach. If the computational domain is split into two subdomains, the Galerkin procedure is applied in each domain, and the jump condition is incorporated into the Galerkin procedure. This will be explained in Sect. 6.

5.2 Perturbed kink behavior with pseudo-spectral method

We first test the Gaussian representation (2) of the Dirac delta. In (25), δ_N becomes the diagonal matrix

$$\delta_N = \mathrm{diag}\left(\delta_\sigma(x_0), \dots, \delta_\sigma(x_N)\right). \tag{27}$$

Figure 7 shows the numerically determined critical velocity $V_{\mathrm{cr}}^{(\mathrm{num})}$ and the absolute error $E = |V_{\mathrm{cr}}^{(\mathrm{num})} - V_{\mathrm{cr}}|$ as a function of N and σ. As in Fig. 4, the continuum limit corresponds to the limit $(1/N, \sigma) \to 0$ (the point at infinity in the lower left corner of the plots), and the error should therefore vanish in this limit. Indeed, as with finite differences, if one increases N while σ is fixed, $V_{\mathrm{cr}}^{(\mathrm{num})}$ converges to a finite value, which in turn converges to V_{cr} as $\sigma \to 0$. As with finite differences, however, if one decreases σ while N is fixed, eventually one reaches a

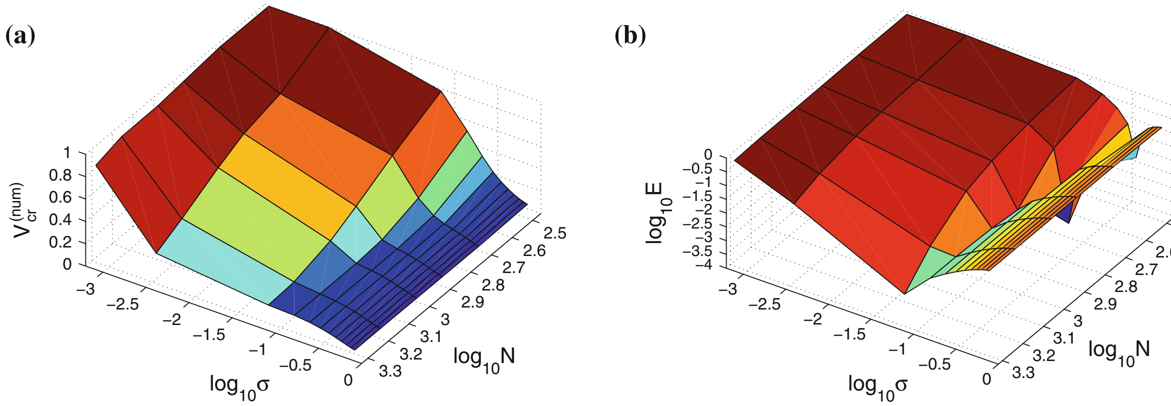

Fig. 7 Numerical critical velocity (**a**) and absolute error $E = |V_{cr}^{(num)} - V_{cr}|$ in value of critical velocity (**b**) for Chebyshev spectral collocation method with Gaussian delta function as a function of N and σ

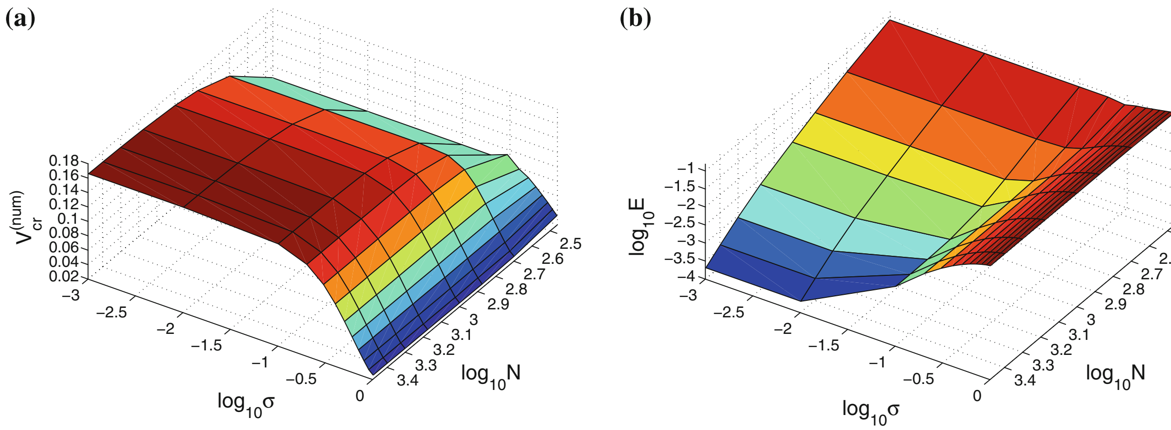

Fig. 8 Same as Fig. 7, but for the Chebyshev spectral collocation method with self-consistent delta

value at which the perturbing term becomes effectively a point source – again with the wrong normalization. If σ is further decreased with N fixed, no limit behavior emerges for the critical velocity, in the sense that $V_{cr} \to 1$, and the system ceases to display any particle passes. More specifically, one needs to use at least a five-point Gaussian to recover the correct behavior in the limit $N \to \infty$.

Note that the need to have enough spatial resolution to resolve the Gaussian delta adequately imposes a much heavier burden for the pseudo-spectral method than for the finite difference method, since the computational cost of implementing pseudo-spectral methods is $O(N^2)$ compared to $O(N)$ for finite differences, and therefore pseudo-spectral methods are typically advantageous when one can use a much smaller number of points compared to what is necessary with finite differences. This problem is further compounded by the fact that the grid spacing in the pseudo-spectral method is nonuniform and is largest near the origin, where the delta is localized.

We next consider the pseudo-spectral method with the self-consistent representation (19) of the Dirac delta. That is, we take

$$\delta_N = \mathrm{diag}\big(\mathrm{D}_N \big(H_\sigma(x_0), \ldots, H_\sigma(x_N)\big)^{\mathrm{T}}\big),$$

where again D_N is the Chebyshev differentiation matrix, and $H_\sigma(x)$ is as in (20).

As before, Fig. 8 shows the dependence on N and σ of the numerical velocity $V_{cr}^{(num)}$ and the absolute error $E = |V_{cr}^{(num)} - V_{cr}|$. As with the finite-difference method, this case is very different from that of the Gaussian representation. That is, a critical velocity is obtained even when taking $\sigma = 0$, and the correct limit is recovered as $N \to \infty$. Again, this is related to the fact that, even when $\sigma = 0$, the perturbing term is not a point source.

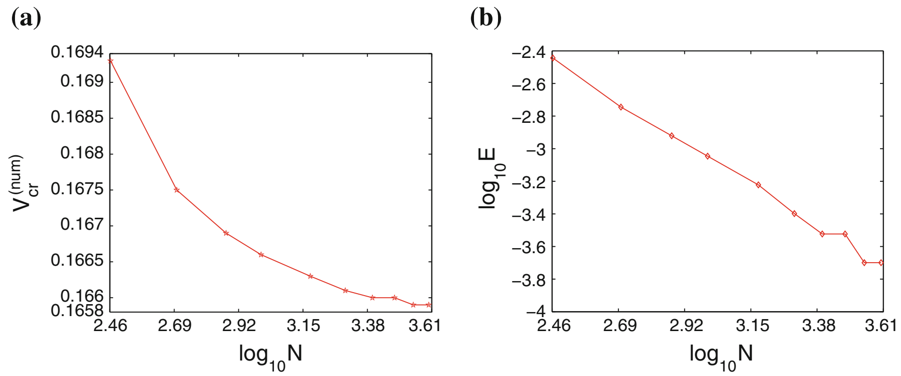

Fig. 9 Numerical critical velocity (**a**) and absolute error (**b**) for Chebyshev spectral collocation method with point source as a function of N

Comparing Figs. 5 and 8, however, one sees that, in order for the error to reach the error floor of 10^{-4}, one should take comparable numbers of spatial grid points in the finite-difference and pseudo-spectral methods, again voiding the advantage of the latter over the former.

Finally, we study perturbed behavior with pseudo-spectral methods when the Dirac delta is modeled by a point source using (5), with $\sigma = \Delta x_{N/2}/2 = (x_{N/2+1} - x_{N/2-1})/4$. Figure 9 shows the dependence on N of the numerical critical velocity and absolute error. As N increases, $V_{cr}^{(num)}$ converges to the correct value. Note, however, that the convergence rate is only linear with N, negating the spectral convergence of the method for the unperturbed equation.

From Figs. 7–9 we see that the self-consistent approach and the point source approach are superior to the Gaussian approximation method. It is also interesting that the point source approach with the spectral method still yields stable and accurate results. Among these three approaches, the self-consistent approach yields the best performance. The overall order of convergence for the self-consistent method is approximately 2.78 when $\sigma \simeq 10^{-3}$, and that for the point source approach is approximately 1.2.

6 Domain decomposition methods

As discussed earlier, when using domain decomposition methods one divides the original domain into two subdomains, $[-L, 0]$ and $[0, L]$, and solves the unperturbed sG equation in each domain. That is, the solutions in the left subdomain and the right subdomain, denoted respectively as $u^{\mp}(x, t)$, satisfy

$$u^-_{tt} - u^-_{xx} + \sin u^- = 0, \qquad -L < x < 0, \tag{28}$$

$$u^+_{tt} - u^+_{xx} + \sin u^+ = 0, \qquad 0 < x < L. \tag{29}$$

At the intersection of the two subdomains, one has the continuity condition (8) together with the jump condition (4). At the outer boundaries of the two subdomains, one has the right and left BCs (17) and (18), and the ICs in each subdomain are simply the restrictions of (10). In each subdomain, either the finite-difference method or the Chebyshev spectral collocation method can be used to solve (28) and (29).

6.1 Domain decomposition with finite-difference method

We use the same uniform spatial grid size $\Delta x = 2L/N$ in each interval $[-L, 0]$ and $[0, L]$, obtaining $N/2+1$ grid points in each subdomain. Explicitly, one has $x_n^- = -L + n\Delta x$ for $n = 0, \ldots, N/2$ on $[-L, 0]$ and $x_n^+ = n\Delta x$ for $n = 0, \ldots, N/2$ on $[0, L]$. The corresponding representations for the solutions in the two subdomains are $u_n^{\pm,k} = u^{(\text{num})}(x_n^\pm, t_k)$. Note that there are only $N+1$ spatial points (not $N+2$) since $x_{N/2}^- = x_0^+ = 0$.

Discretizing the equation at the kth time step and utilizing the three-point centered stencil for the second derivatives we obtain, for $k \geq 1$ and $n = 1, 2, \ldots, N/2 - 1$,

$$\frac{u_n^{\pm,k+1} - 2u_n^{\pm,k} + u_n^{\pm,k-1}}{\Delta t^2} - \frac{u_{n+1}^{\pm,k} - 2u_n^{\pm,k} + u_{n-1}^{\pm,k}}{\Delta x^2} + \sin u_n^{\pm,k} = 0.$$

The initial and left BCs are imposed in a straightforward way. For the right boundary we use the explicit scheme, similarly to what was done in Sect. 4:

$$\frac{u_{N/2}^{+,k+1} - u_{N/2}^{+,k}}{\Delta t} + \frac{u_{N/2}^{+,k} - u_{N/2-1}^{+,k}}{\Delta x} = 0. \tag{30}$$

From the continuity condition (8) we have

$$u_0^{+,k} = u_{N/2}^{-,k}. \tag{31}$$

Moreover, the jump condition (4) needs to be discretized as well. For this purpose, we use a higher-order approximation for the derivative term using Lagrange interpolation polynomials. For example, for the solution near $x = x_{N/2}^-$ in the left domain, $u^-(x,t)$, the Lagrange interpolation based on $p \geq 1$ points including $u^-(0^-, t)$ is given by

$$u^-(x,t) = \sum_{i=N/2-p}^{N/2} u^-(x_i,t) l_i(x) = \sum_{i=N/2-p}^{N/2} u^-(x_i,t) \prod_{N/2-p \leq m \leq N/2,\, m \neq i} \frac{x - x_m}{x_i - x_m}.$$

The derivative of $u^-(x,t)$ at $x = x_{N/2}^-$ is then given by

$$\left.\frac{\mathrm{d}u^-(x,t)}{\mathrm{d}x}\right|_{x=x_{N/2}^-} = \sum_{i=N/2-p}^{N/2} u^-(x_i,t) l_i'(x_{N/2}^-).$$

For example, if we choose $p = 2$, which yields second-order accuracy, we get

$$\left.\frac{\mathrm{d}u^-(x,t)}{\mathrm{d}x}\right|_{x=x_{N/2}^-} = \frac{1}{\Delta x}\left[\frac{3}{2}u_{N/2}^{-,k} - 2u_{N/2-1}^{-,k} + \frac{1}{2}u_{N/2-2}^{-,k}\right].$$

Similarly,

$$\left.\frac{\mathrm{d}u^+(x,t)}{\mathrm{d}x}\right|_{x=x_0^+} = \frac{1}{\Delta x}\left[-\frac{3}{2}u_0^{+,k} + 2u_1^{+,k} - \frac{1}{2}u_2^{+,k}\right].$$

Using $u_{N/2}^{-,k} = u_0^{+,k}$ with the jump condition (4), we then have

$$\frac{1}{\Delta x}\left[-3u_0^{+,k+1} + 4u_1^{+,k+1} - u_2^{+,k+1}\right] = -\epsilon \Delta x\, \sin u_0^{+,k+1} = -\epsilon \Delta x\, \sin u_{N/2}^{-,k+1}. \tag{32}$$

The last condition provides a nonlinear equation for the unknown value $u_0^{+,k+1} = u_{N/2}^{-,k+1}$, which we solve using Newton's method to obtain the updated value of the solution at $x = 0$, i.e., $u(0,t)$.

As before, we first test the domain decomposition method on the unperturbed sG equation (7). We find that the error in the numerically measured velocity of a kink is less than 10^{-4} when $L = 80$, $\Delta t = 2 \times 10^{-4}$, and $N \geq 8{,}000$. We then compute the numerical critical velocity $V_{\mathrm{cr}}^{(\mathrm{num})}$ and the absolute error $E = |V_{\mathrm{cr}}^{(\mathrm{num})} - V_{\mathrm{cr}}|$ as a function of N. The results are shown in Fig. 10. It appears that the numerical critical velocity converges to the PDE value with an overall convergence order of approximately 2.9, which is a better order than the single-domain case.

6.2 Domain decomposition with Chebyshev spectral collocation method

We introduce the spectral collocation points in each subdomain $[-L, 0]$ and $[0, L]$ as follows: for $n = 0, \ldots, N/2$

$$x_n^- = -\frac{L}{2}[1 + \cos(2n\pi/N)], \qquad x_n^+ = \frac{L}{2}[1 - \cos(2n\pi/N)].$$

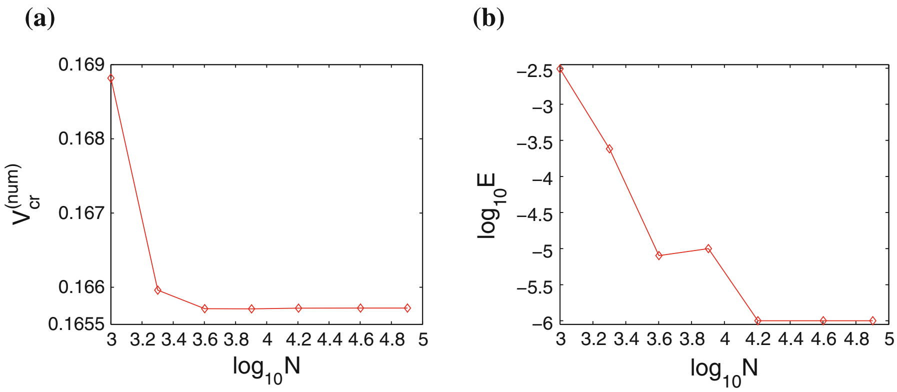

Fig. 10 Numerical critical velocity $V_{\mathrm{cr}}^{(\mathrm{num})}$ (**a**) and absolute error (**b**) for domain decomposition with finite differences as a function of N

Again, $x_{N/2}^- = x_0^+ = 0$. Hence, there is a total of $(N+1)$ collocation points on $[-L, L]$, as before. We then define the corresponding Chebyshev polynomials:

$$\phi_n^-(x) = T_n(\xi^-(x)), \qquad \phi_n^+(x) = T_n(\xi^+(x)), \qquad n = 0, \ldots, N/2,$$

where $\xi^\pm(x)$ map the intervals $[0, L]$ and $[-L, 0]$ into $[-1, 1]$, and $T_n(\xi)$ is defined as before. Explicitly, $\xi^-(x) = 2x/L + 1$, $\xi^+(x) = 2x/L - 1$. The approximations to the solution in the two subdomains are then represented by

$$u^-(x,t) = \sum_{n=0}^{N/2} \hat{u}_n^-(t)\phi_n^-(x) \qquad \text{and} \qquad u^+(x,t) = \sum_{n=0}^{N/2} \hat{u}_n^+(t)\phi_n^+(x).$$

From (1) we then obtain

$$\frac{\mathbf{u}^{\pm,k+1} - 2\mathbf{u}^{\pm,k} + \mathbf{u}^{\pm,k-1}}{\Delta t^2} - \mathrm{D}_N^2 \mathbf{u}^{\pm,k} + \sin \mathbf{u}^{\pm,k} = 0,$$

where $\mathbf{u}^{\pm,k} = (u_0^{\pm,k}, \ldots, u_N^{\pm,k})^{\mathrm{T}}$, with $u_n^{\pm,k} = u^{(\mathrm{num})}(x_n^\pm, t_k)$. As with domain decomposition using the finite-difference method, the IC and the BC at $x = -L$ are imposed in a straightforward way. For the right BC, similarly to Sect. 5, we use the explicit scheme (30), where now $\Delta x = x_{N/2}^+ - x_{N/2-1}^+$.

The discretization of the jump condition (4) with the Chebyshev method is given by

$$D_N u^{+,k}\Big|_{x_0^+} - D_N u^{-,k}\Big|_{x_{N/2}^-} = -\epsilon \sin\left(u^{+,k}(x_0^+)\right).$$

Let $v = u_{N/2}^{-,k+1} = u_0^{+,k+1}$. Then, using the elements of the derivative matrix D, we obtain

$$(D_{0,0} - D_{N/2,N/2})v + \epsilon \sin(v) = \sum_{j=0}^{N/2-1} D_{N/2,j} u_j^{-,k+1} - \sum_{j=1}^{N/2} D_{0,j} u_j^{+,k+1} = 0,$$

where $D_{i,j}$ denote the entries of D_N. We solve the preceding equation using Newton's method for v, as was done for the finite-difference method.

Again, we first test the method on the unperturbed sG equation (7). We find that the error in the numerically measured velocity is less than 10^{-4} for $L = 80$, $N \geq 500$, and $\Delta t = 2 \times 10^{-4}$. We then compute the dependence on N of the numerical critical velocity $V_{\mathrm{cr}}^{(\mathrm{num})}$ and the absolute error $E = |V_{\mathrm{cr}}^{(\mathrm{num})} - V_{\mathrm{cr}}|$. The results, shown in

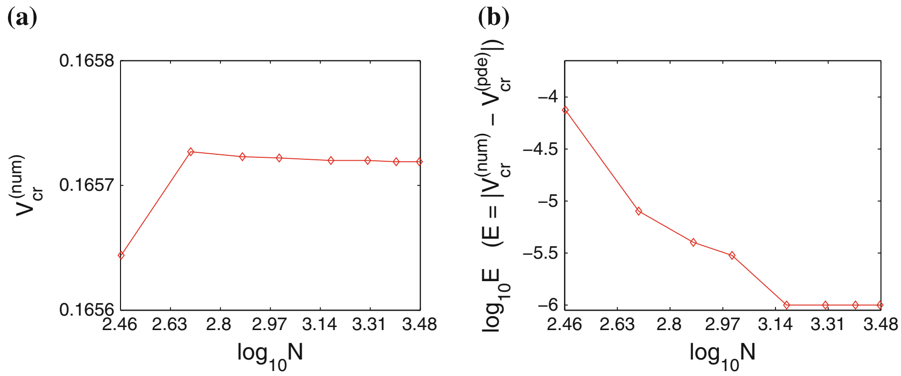

Fig. 11 Same as Fig. 10, but for domain decomposition with Chebyshev pseudo-spectral method

Fig. 11, demonstrate that the numerical critical velocity converges to that of the PDE value with a convergence order of approximately 2.

6.3 Domain decomposition with semi-implicit methods

The domain decomposition method (as well as the one-domain approach with the Galerkin projection of the Dirac delta) can be more efficiently implemented using a semi-implicit scheme. For this purpose, consider the Legendre approximation of the solution, $u_N(x,t)$, as a polynomial of degree at most N such that

$$u(x,t) = \sum_{l=0}^{N} \hat{u}_l(t) L_l(\xi(x)),$$

where $L_l(\xi)$ is the Legendre polynomial of degree l and ξ is the linear mapping $\xi : x \to [-1,1]$, i.e., $x = L\xi$. Using this expression in (1) yields

$$\sum_{l=0}^{N} \frac{\mathrm{d}^2\hat{u}_l(t)}{\mathrm{d}t^2} L_l(\xi(x)) = \frac{1}{L^2} \sum_{l=0}^{N} \hat{u}_l(t) L_l''(\xi(x)) - \sin(u(x,t)),$$

where the prime denotes derivative with respect to ξ, and where we used $\mathrm{d}\xi/\mathrm{d}x = 1/L$. Using the Galerkin projection onto $L_{l'}(\xi)$ and the orthogonality of $L_l(x)$ and $L_{l'}(x)$ for $l \neq l'$ we obtain

$$\frac{\mathrm{d}^2\hat{u}_l(t)}{\mathrm{d}t^2} = \frac{1}{L^2} \sum_{l=0}^{N} \hat{u}_l(t) \frac{2l'+1}{2} \int_{-1}^{1} L_l''(\xi) L_{l'}(\xi)\mathrm{d}\xi - \frac{2l'+1}{2} \int_{-1}^{1} \sin(u(x,t)) L_{l'}(\xi)\mathrm{d}\xi.$$

Define the column vector $\hat{\mathbf{u}} = (\hat{u}_0, \ldots, \hat{u}_N)^{\mathrm{T}}$, as well as the matrix $A = (A_{l',l})$, and the column vector $\mathbf{b} = (b_{l'})$ as

$$A_{l',l} = \frac{2l'+1}{2} \int_{-1}^{1} L_l''(\xi) L_{l'}(\xi)\mathrm{d}\xi, \qquad b_{l'} = -\frac{2l'+1}{2} \int_{-1}^{1} \sin(u(x,t)) L_{l'}(\xi)\mathrm{d}\xi.$$

The semi-implicit scheme employs an implicit scheme for the linear part of the equation and an explicit scheme for the nonlinear part of the equation as follows:

$$\frac{\hat{\mathbf{u}}^{n+1} - 2\hat{\mathbf{u}}^n + \hat{\mathbf{u}}^{n-1}}{\Delta t^2} = \frac{1}{L^2} A\hat{\mathbf{u}}^{n+1} + \mathbf{b}^n.$$

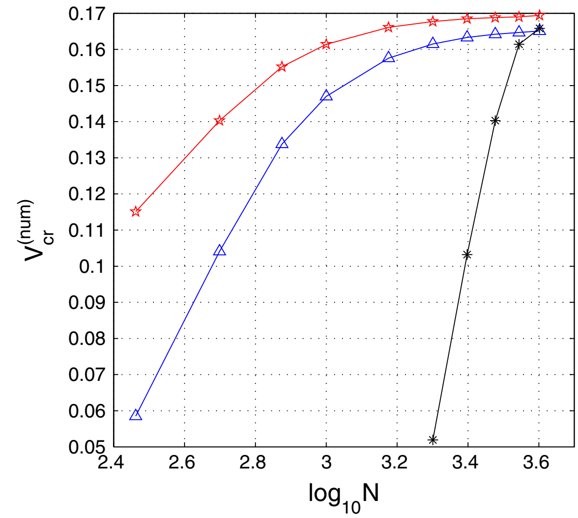

Fig. 12 Critical velocity versus N with explicit and implicit methods. *Red stars*: Gaussian with three points (explicit); *blue triangles*: Gaussian with five points (explicit scheme); *black asterisks*: Gaussian with five points (implicit scheme). (Color figure online)

Thus, $\hat{\mathbf{u}}^{n+1}$ can be obtained as $\hat{\mathbf{u}}^{n+1} = U^{-1}(2\hat{\mathbf{u}}^n - \hat{\mathbf{u}}^{n-1} + \Delta t^2\mathbf{b}^n)$, where $U = I - (\Delta t/L)^2 A$. The complexity of computing U^{-1} can be reduced using the structure of A so that the actual algorithm is implemented efficiently.

Figure 12 shows the critical velocity versus N with different methods: the three- (red) and five-point (blue) Gaussian approximation for the explicit scheme and the five-point Gaussian (black) approximation for the implicit scheme. Here we note that, although the implicit scheme can be computed efficiently with a lower computational complexity, the overall performance is similar to that of the explicit scheme when N is large. We also note that the explicit (collocation) method is also implemented efficiently via FFT.

7 Comparisons and discussion

We have investigated the convergence properties of different combinations of numerical methods for the perturbed sG equation (1) with Dirac delta forcing. The numerical results show that (1) in general, when one has a parameter σ governing the representation of the Dirac delta, one must be careful when taking the limit $1/N, \sigma \to 0$ to recover the correct PDE behavior. This is similar to the situation with the limit $\Delta x, \Delta t \to 0$; (2) in particular, when using the Gaussian delta, for both the finite-difference and pseudo-spectral methods, one must make sure that the support of the delta is nonzero on at least five grid points; otherwise the results do not converge to the correct continuum limit; (3) spectral methods over the whole domain with the Gaussian and self-consistent delta representations are not advantageous due to the large number of points that are needed anyway to resolve the delta.

Further insight can be obtained by combining the results of the previous sections. Figure 13 shows the dependence of the absolute error E on N for the finite-difference method (Figure 13a) and the pseudo-spectral method (Figure 13b) in combination with the various representations of the Dirac delta. The results show that all methods require a significant number of grid points to properly resolve the critical behavior of the kink solutions. Among all the combinations, domain decomposition methods, in conjunction with both finite-difference methods and spectral methods, seem best. For both finite-difference and spectral methods, the Gaussian approximation method (which is the most commonly used method in the optics community) is inferior, in the sense that it requires significantly higher grid resolutions than other methods to attain the same level of accuracy. It is interesting to see that, even though the point source approach generates a Gibbs phenomenon in the solution, it yields accurate results for the critical velocity with both finite-difference and spectral methods. The self-consistent method yields results similar to those of the Gaussian method, but its convergence rate is slightly higher and its performance improves compared to other methods as N gets large. Overall, the Gaussian representation and the self-consistent representation yield similar results for both the finite-difference and spectral methods.

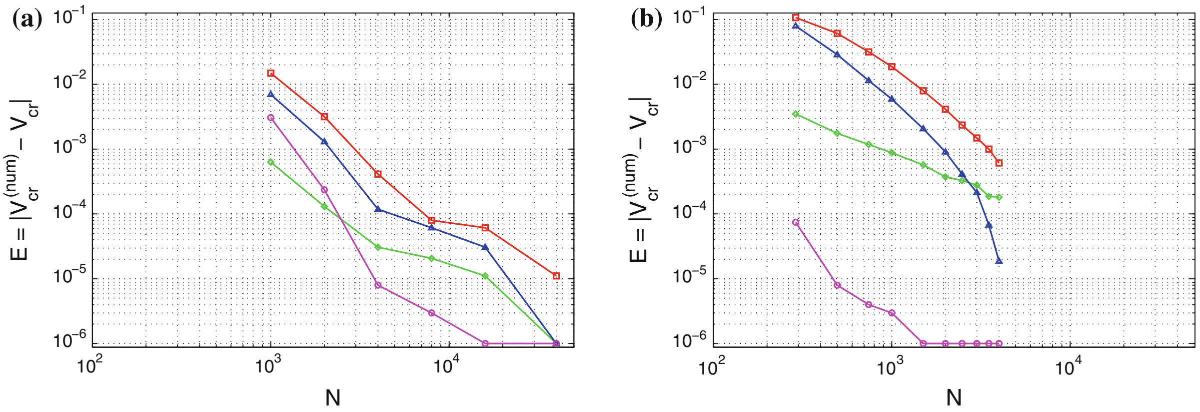

Fig. 13 Absolute error in value of critical velocity with finite-difference methods (**a**) or pseudo-spectral methods (**b**) as a function of N for different representations of the Dirac delta. *Red*: Gaussian with five points; *green*: point source; *blue*: self-consistent with $\sigma = 0$; *magenta*: domain decomposition. (Color figure online)

We should note that an accurate and efficient method of finding the critical velocity with high precision was recently proposed for the sG equation in [27] and for the nonlinear Schrödinger equation in [28] using the generalized polynomial chaos method. Also, other methods are of course available to integrate the sG equation numerically, for example, completely integrable schemes [20,29] and Galerkin methods [23–25]. Here we chose to limit ourselves to the most widely used spatial discretization methods: the finite-difference and pseudo-spectral methods. The study of other methods remains a subject for future work.

Acknowledgments We thank Roy Goodman, Panayotis Kevrekidis, and Jingbo Xia for many valuable discussions. This study was partially supported by the National Science Foundation under Award Number DMS-0908399.

References

1. Scott AC, Chu FYF, McLaughlin DW (1973) The soliton: a new concept in applied science. Proc IEEE 61:1443–1483
2. Ablowitz MJ, Segur H (1981) Solitons and the inverse scattering transform. SIAM, Philadelphia
3. Fei Z (1992) Y S Kivshar and L Vázquez, Resonant kink–impurity interaction in the sine-Gordon model. Phys Rev A 45:6019–6030
4. Forinash K, Peyrard M, Malomed BA (1994) Interaction of discrete breathers with impurity modes. Phys Rev E 49:3400–3411
5. Cao XD, Malomed BA (1995) Soliton-defect collisions in the nonlinear Schrödinger equation. Phys Lett A 206:177–182
6. Ernst T, Brand J (2010) Resonant trapping in the transport of a matter-wave soliton through a quantum well. Phys Rev A 81(033614):1–11
7. Goodman RH, Holmes PJ, Weinstein MI (2002) Interaction of sine-Gordon kinks with defects: phase space transport in a two-mode model. Physica D 161:21–44
8. Goodman RH, Slusher RE, Weinstein MI (2002) Stopping light on a defect. J Opt Soc Am B 19:1635–1652
9. Goodman RH, Haberman R (2004) Interaction of sine-Gordon kinks with defects: the two-bounce resonance. Physica D 195:303–323
10. Goodman RH, Haberman R (2007) Chaotic scattering and the n-bounce resonance in solitary–wave interactions. Phys Rev Lett 98(104103):1–4
11. Fratalocchi A, Assanto G (2007) Symmetry-breaking instabilities in perturbed optical lattices: nonlinear nonreciprocity and macroscopic self-trapping. Phys Rev A 75(063828):1–5
12. Mak WCK, Malomed BA, Chu PL (2003) Interaction of a soliton with a local defect in a Bragg grating. J Opt Soc Am B 20:725–735
13. Morales-Molina L, Vicencio RA (2006) Trapping of discrete solitons by defects in nonlinear waveguides arrays. Opt Lett 31:966–968
14. Pando CL, Doedel EJ (2005) Onset of chaotic symbolic synchronization between population inversions in an array of weakly coupled Bose–Einstein condensates. Phys Rev E 71(5 Pt 2): 056201
15. Peyrard M, Kruskal MD (1984) Kink dynamics in the highly discrete sine-Gordon system. Physica D 14:88–102
16. Piette B, Zakrzewski WJ (2007) Scattering of sine-Gordon kinks on potential wells. J Phys A 40(5995):1–16
17. Soffer A, Weinstein MI (2005) Theory of nonlinear dispersive waves and selection of the ground state. Phys Rev Lett 95(213905):1–4
18. Trombettoni A (2003) Discrete nonlinear Schrödinger equation with defects. Phys Rev E 67(016607):1–11

19. Friedlander FG, Joshi MS (1998) Introduction to the theory of distributions. Cambridge University Press, Cambridge
20. Ablowitz MJ, Herbst BM, Schober CM (1995) Numerical simulation of quasi-periodic solutions of the sine-Gordon equation. Phycica D 87:37–47
21. Jung J-H, Don WS (2009) Collocation methods for hyperbolic partial differential equations with singular sources. Adv Appl Math Mech 1:769–780
22. Boyd JP (2001) Chebyshev and Fourier spectral methods. Dover, New York
23. B Fornberg (1998) A practical guide to pseudospectral methods. Cambridge Universiy Press, Cambridge
24. Gottlieb D (1977) Numerical analysis of spectral methods: theory and applications. SIAM, Philadelphia
25. Hesthaven JS, Gottlieb S, Gottlieb D (2007) Spectral methods for time-dependent problems. Cambridge Universiy Press, Cambridge
26. Trefethen LN (2000) Spectral methods in Matlab. SIAM, Philadelphia
27. Chakraborty D, Jung J-H (2013) Efficient determination of the critical parameters and the statistical quantities for Klein–Gordon and sine-Gordon equations with a singular potential using generalized polynomial chaos methods. J Comput Sci 4:46–61
28. Chakraborty D, Jung J-H, Lorin E (2013) Efficient determination of critical parameters of nonlinear Schrödinger equation with point-like potential using generalized polynomial chaos methods. App Numer Math 72:115–130
29. Faddeev LD, Takhtajan LA (1987) Hamiltonian methods in the theory of solitons. Springer, New York